ACS OMEGA

Open Access

http://pubs.acs.org/journal/acsodf

Article

Facile Hydrothermal Synthesis of $BiVO_4$/MWCNTs Nanocomposites and Their Influences on the Biofilm Formation of Multidrug Resistance *Streptococcus mutans* and *Proteus mirabilis*

Zeena R. Rhoomi, Duha S. Ahmed,* Majid S. Jabir,* Balamuralikrishnan Balasubramanian, Maged A. Al-Garadi, and Ayman A. Swelum*

Cite This: *ACS Omega* 2023, 8, 37147−37161

Read Online

ACCESS | Metrics & More | Article Recommendations

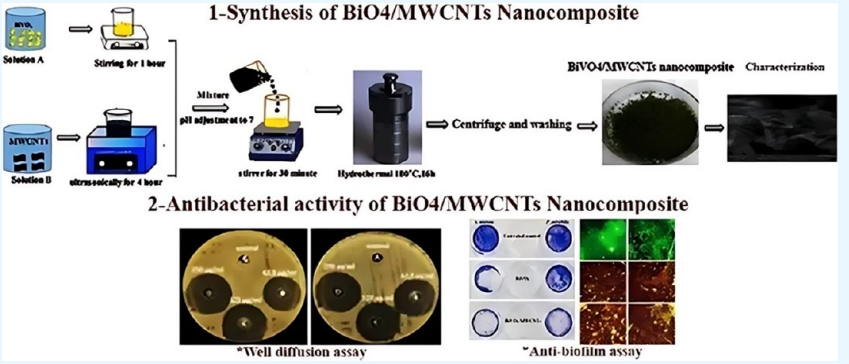

ABSTRACT: This study utilized a simple hydrothermal technique to prepare pure $BiVO_4$ and tightly bound $BiVO_4$/multiwalled carbon nanotubes (MWCNTs) nanocomposite materials. The surfactant was employed to control the growth, size, and assembly of $BiVO_4$ and the nanocomposite. Various techniques including X-ray diffraction (XRD), Ultraviolet−visible (UV−vis), photoluminescence (PL), Raman, transmission electron microscopy (TEM), scanning electron microscopy (SEM), and energy-dispersive X-ray spectroscopy (EDS) were utilized to analyze and characterize $BiVO_4$ and the $BiVO_4$/MWCNTs nanocomposite. Through XRD analysis, it was found that the carbon nanotubes were effectively embedded within the lattice of $BiVO_4$ without generating any separate impurity phase and had no influence on the $BiVO_4$ monoclinic structure. TEM images confirmed the presence of MWCNTs within $BiVO_4$. Furthermore, adding MWCNTs in the $BiVO_4$/MWCNTs nanocomposite resulted in an effective charge transfer transition and improved carrier separation, as evidenced by PL analysis. The introduction of MWCNTs also led to a significant reduction in the optical band gap due to quantum effects. Finally, the antibacterial activity of pure $BiVO_4$ and the $BiVO_4$/MWCNTs nanocomposite was assessed by exposing *Proteus mirabilis* and *Streptococcus mutans* to these materials. Biofilm inhibition and antibiofilm activity were measured using a crystal violet assay and a FilmTracer LIVE/DEAD Biofilm Viability Kit. The results demonstrated that pure $BiVO_4$ and $BiVO_4$/MWCNTs effectively inhibited biofilm formation. In conclusion, both pure $BiVO_4$ and $BiVO_4$/MWCNTs are promising materials for inhibiting the bacterial biofilm during bacterial infections.

1. INTRODUCTION

The nanoparticles in the range of 1−100 nm have attracted research interest because of their specific physical properties and reactivity depending on their size. These nanoparticles have been used in a wide range of fields such as cosmetics, textile manufacturing, and biomedical applications.[1] Among metallic oxide nanoparticles, semiconductor-based photocatalysts have received significant attention due to their various shape-dependent characteristics, low cost, chemical stability, and environmentally friendly features.[2−4] In the areas of water treatment, food production, biomedical, and environmental fields, nanocomposites are highly significant. These newly discovered materials have a rapid role in inhibiting bacteria development and help in the fight against antibiotic-resistant bacteria in the healthcare system.[5,6] However, most metal binary oxides suffer from limited response to visible light due to their large band gap ($E_g > 3$ eV), such as TiO_2 and ZnO. Other studies are exploring new narrow-band-gap semiconductors, such as bismuth-based semiconductors, because they are chemically

Received: July 2, 2023
Accepted: September 15, 2023
Published: September 28, 2023

stable and nontoxic and exhibit visible light photocatalytic properties.[7−9] Among the semiconductor photocatalysts, bismuth vanadate $BiVO_4$ has received a great deal of research interest due to its distinct physical and chemical features, including its ability to degrade substances and pathogens in water treatment, its role as an antimicrobial agent, and its nontoxicity for cells in biomedical applications.[10−13] The narrow band gap (2.4 eV) and suitable band positions of $BiVO_4$ make it an excellent photocatalyst under sunlight.[14−19] Various methods have been used to synthesize $BiVO_4$, such as sol−gel, precipitation, and microwave synthesis.[20−22] In recent years, the hydrothermal method has been widely used to create bismuth complexes due to its moderate preparation conditions, such as a relatively low temperature, short reaction time, controllable pH, and other factors. Furthermore, the hydrothermal method allows for easy control of parameters that affect photocatalyst performance, such as crystal structure, morphology, and band gap.[23] One-dimensional multiwalled carbon nanotubes (MWCNTs) have gained interest due to their outstanding mechanical, electrical, and optical properties.[24−30] MWCNTs have been used in recent research due to their excellent adsorption capacity and chemical stability. The cytotoxicity and low dispersion of MWCNTs can be overcome by oxidizing them, which reduces toxicity, increases solubility, and improves interaction with nanoparticles and organisms. Due to their higher electron-transfer ability, MWCNTs support charge separation, leading to improved photocatalytic activity in pollution removal.[31] MWCNTs also increase the absorption of visible light by reducing the band gap of $BiVO_4$. Additionally, 1D MWCNTs reduce transmission distance and promote electron transfer, inhibiting the recombination of electron−hole carriers.[32,33] Moreover, MWCNTs offer more active positions due to their greater specific surface area and enhance the adsorption of nanocomposites.[34−36] This study focuses on the effect of introducing functionalized MWCNTs into $BiVO_4$ using the hydrothermal method and their application in antibacterial activity. The investigation and analysis highlight the potential of these nanocomposites by studying their size, morphology, and microstructure before and after embedding MWCNTs using X-ray diffraction (XRD), ultraviolet−visible (UV−vis), Raman, and transmission electron microscopy (TEM). Finally, the results demonstrate that both pure $BiVO_4$ nanocomposites and nanocomposites with MWCNTs exhibit antibacterial efficiency against the studied bacterial strains. The findings suggest that the prepared nanoparticles have potential as antimicrobial and biofilm inhibition agents in the biomedical field.

2. MATERIALS AND METHODS

2.1. Materials. Bismuth(III) nitrate pentahydrate ($Bi(NO_3)_3{\cdot}5H_2O$) with a purity of 98% was purchased from Sigma-Aldrich, a company in Germany. Ammonium metavanadate (NH_4VO_3) with a purity of 99% was purchased from glentham.com, a company in the United Kingdom. Sodium hydroxide (NaOH) was purchased from Chemical Reagent Company, a company in China. Multiwalled carbon nanotubes (MWCNTs) with a purity greater than 95 wt % and a diameter of 8−15 nm were purchased from Grafton Company, a company in the USA. Nitric acid (HNO_3) with a purity of 69% was purchased from CDH, a company in India. Deionized water was used throughout the experiment.

2.2. Synthesis of $BiVO_4$ and $BiVO_4$/MWCNTs Nanocomposite. Pure $BiVO_4$ was synthesized using a hydrothermal method.[37−39] First, 2 mmol of $Bi(NO_3)_3{\cdot}5H_2O$ and 4 mL of 4 mol/L HNO_3 were dissolved in 50 mL of distilled water and stirred for 30 min to form solution A. Second, 2 mmol of (NH_4VO_3) and 4 mL of 2 mol/L NaOH were dissolved in water and stirred for 30 min to form solution B. The two solutions were then mixed and placed in a Teflon-lined autoclave, which was sealed and heated in an oven at 180 °C for 16 h. The resulting yellow precipitate of $BiVO_4$ was cleaned with ethanol and distilled water and then heated in a convection oven at 60 °C for 12 h. The same procedure was used to synthesize the $BiVO_4$/MWCNTs nanocomposite, with the addition of 0.64 g of $Bi(NO_3)_3{\cdot}5H_2O$, 0.12 g of NH_4VO_3, 0.4 g of functionalized MWCNTs, and 0.3 g of SDS dispersed in 100 mL of deionized water.

2.3. Characterization. The structure of the $BiVO_4$ and $BiVO_4$/MWCNTs nanocomposite products was analyzed using XRD analysis (X-ray Diffraction 6000, Shimadzu) with CuK radiation (λ = 1.542), and the data were recorded in a 2θ range of 10−70°. The optical properties and band gaps were measured using UV−visible spectroscopy (Shimadzu UV-1800 spectrophotometer). Photoluminescence (PL) spectroscopy was performed using a monochromatic excitation wavelength of about 250 nm (Cary Eclipse fluorescence model, Iran) at room temperature to analyze the emission wavelengths of $BiVO_4$ and the $BiVO_4$/MWCNTs nanocomposite in the range of 200−800 nm. Transmission electron microscopy (TEM, Philips-EM-208S) was used to visualize the surface morphology and size of the $BiVO_4$ and $BiVO_4$/MWCNTs samples, while scanning electron microscopy (SEM Apreo2, Thermo Fisher Scientific) was used to visualize the efficiency of the samples on bacterial cells. Energy-dispersive X-ray spectroscopy (EDS) was used for elemental analysis.

2.4. Antibacterial Activity Test. The antibacterial activity of pure $BiVO_4$ and the $BiVO_4$/MWCNTs nanocomposite was investigated against *P. mirabilis* and *S. mutans* using an agar well diffusion assay.[40,41] Different concentrations (62.5, 125, 250 μg/mL) of the bacterial samples were cultivated at 37 °C overnight on Muller−Hinton (MH) agar (HiMedia, India) containing pure $BiVO_4$ and the $BiVO_4$/MWCNTs nanocomposite, and the average diameter of inhibition zones were recorded.[42] The minimum inhibitory concentration (MIC) was measured by using a serial dilution method following the NCCLS guidelines. A colony-forming unit (2×10^6 CFU/mL) was inoculated in 96-well microplates, containing 100 μL of sterile Lysogenia broth media (HiMedia, India) in the presence of different concentrations of pure $BiVO_4$ and $BiVO_4$/MWCNTs (0.1220−500 μg/mL). DMSO (0.01%) without pure $BiVO_4$ and $BiVO_4$/MWCNTs was used as a negative control.

2.5. Crystal Violet Staining. In this test, *P. mirabilis* and *S. mutans* (1×10^6 CFU/mL) were grown in 24-well plates and treated with pure $BiVO_4$ and the $BiVO_4$/MWCNTs nanocomposite at a concentration of 125 μg/mL for 24 h. After that, the samples were washed with PBS, and *P. mirabilis*- and *S. mutans*-adhered wells were stained with crystal violet (0.1%, Sigma) after rinsing twice with D.W. To measure biofilm development, 0.2 mL of 95% ethanol was added to crystal violet-stained wells and incubated for 2 h while being shaken. The optical density was then calculated at 595 nm.

2.6. Antibiofilm Activity of Pure $BiVO_4$ and $BiVO_4$/MWCNTs. Biofilms formed on culture dishes of Lysogenia broth medium (HiMedia, India) were untreated (control) or treated with the pure $BiVO_4$ and $BiVO_4$/MWCNTs at a concentration of 125 μg/mL for 24 h and stained using the FilmTracer LIVE/

https://doi.org/10.1021/acsomega.3c04722
ACS Omega 2023, 8, 37147−37161

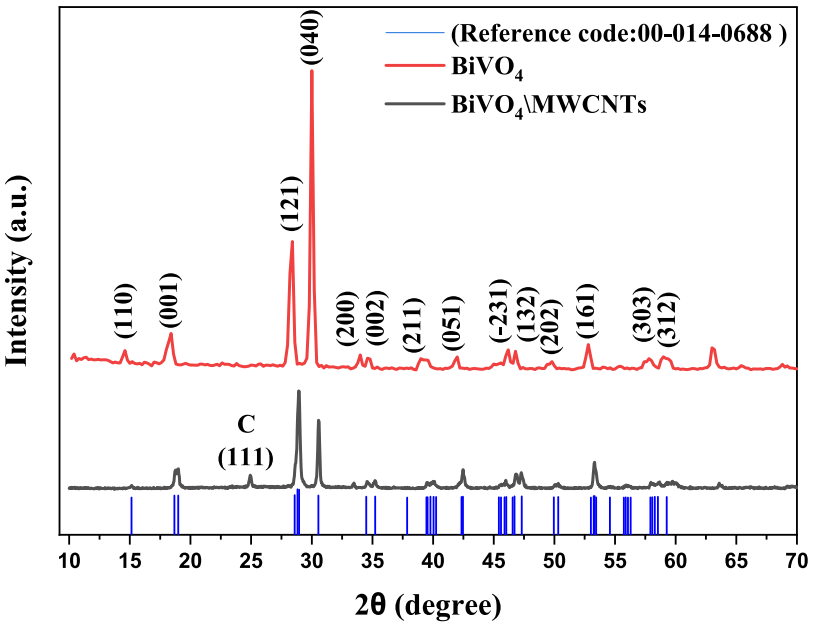

Figure 1. Patterns of XRD of $BiVO_4$ and the $BiVO_4$/MWCNTs nanocomposite with the reference code by using the hydrothermal method.

DEAD Biofilm Viability Kit. The images were captured using a Leica TCS SP5 II confocal microscope.

2.7. Investigation of Biofilm Metabolic Activity. Biofilms were formed in glass tubes in the presence and absence of the pure $BiVO_4$ and $BiVO_4$/MWCNTs samples.[43] After incubation at anaerobic conditions at 37 °C and for 48 h, the biofilm suspension was stained with a Live/Dead stain kit and analyzed by flow cytometry. Briefly, 10 μL of Syto 9 (30 μM) was added for 10 min, and then 10 μL of propidium iodide (500 μM) was added for 10 min; the samples were washed 2 times in PBS and centrifuged for 2 min at 2000 rpm. The sample with two stain components was excited at 488 nm, and the emission was registered using the FITC channel for Syto 9 (530/30) and the (670/LP) channel for propidium iodide. The results of the biofilm cell viability were expressed in the percentage of untreated control cells.

2.8. Statistical Analysis. The data from three independent experiments were represented as mean ± standard deviation. GraphPad Prism (7) was used to carry out the statistical analysis via the application of the one-way ANOVA analysis of variance. p values less than 0.05 were considered significant. *$p < 0.05$, **$p < 0.01$, ***$p < 0.001$, and ****$p < 0.0001$.

3. RESULTS AND DISCUSSION

3.1. Structural, Optical, and Morphological Studies. XRD analysis was performed at room temperature on pure $BiVO_4$ and the $BiVO_4$/MWCNTs nanocomposite. As shown in Figure 1, the formation of the pure $BiVO_4$ monoclinic structure (red line) was confirmed by the diffraction peaks at 2θ = 14.63, 18.33, 28.34, 30.03, 33.83, 34.69, 39.27, 41.91, 46.23, 46.82, 52.77, 57.74, 59.16, and 63.07°, which can be indexed to (110), (001), (121), (040), (200), (002), (211), (051), (−231), (132), (202), (161), (303), and (321) planes, respectively, as consistent with the reference code (JCPDS card no. 014-0,688). Besides, as shown in Figure 1, the new peak formed appears in the nanocomposite (black line) and not in pure $BiVO_4$, which is related to the peak of the plane (111) at 2θ = 24.96° and is attributed to the peak characteristic of the tetragonal structure of MWCNTs. The results reveal that the MWCNTs were successfully embedded inside $BiVO_4$. The Scherrer formula was used to determine the average crystallite size $D = k\lambda/(\beta_{size}\cos\theta)$, where k is the shape factor crystal, λ is the wavelength of Cu−K radiation utilized, and θ is the angle of Bragg. As shown in Table 1, the crystalline size of $BiVO_4$ was smaller than that of the $BiVO_4$/MWCNTs nanocomposite, related to loading MWCNTs into $BiVO_4$, which led to an increase in the crystalline size.[43−45] Besides, increasing the diffusion of Bi^{3+} ions into VO_4^{3-} anions through the crystallization process[43,44] confirms the thermodynamic nucleation.[45] Furthermore, carbon atoms with a relatively higher atomic radius of 0.077 nm replace oxygen atoms with a relatively smaller atomic radius of 0.074 nm.[46] The carbon has been successfully incorporated into the $BiVO_4$ lattice according to XRD measurements. XRD patterns show that a small amount of carbon was effectively integrated into the lattice $BiVO_4$, inducing lattice expansion without generating any separated impurity phase (Table 2).

Table 1. Crystalline Size of Pure $BiVO_4$ and the $BiVO_4$/MWCNTs Nanocomposite by Using the Hydrothermal Method

materials	2θ (deg)	*Hkl*	fwhm (deg)	grain size (nm)	d (A^o)
$BiVO_4$ nanostructure	18.33	001	0.6783	11.86	4.83
	28.34	121	0.5373	15.25	3.14
	30.03	040	0.4626	17.78	2.97
$BiVO_4$/MWCNTs nanocomposite	18.91	001	0.2801	28.75	3.08
	28.93	121	0.2143	38.28	2.92
	30.58	040	0.2326	35.41	1.71

The UV−visible spectroscopy of pure $BiVO_4$ and the $BiVO_4$/MWCNTs nanocomposite was performed in the range of 250−800 nm, as shown in Figure 2. $BiVO_4$ effectively absorbs visible light and operates as a light-driven active photocatalyst for the degradation of organic pollutants, as demonstrated in Figure 2(a), where a strong optical absorption is visible in a wavelength larger than 420 nm. As can be seen, pure $BiVO_4$ samples have an absorption edge of around 466 nm and are yellowish-colored

https://doi.org/10.1021/acsomega.3c04722
ACS Omega 2023, 8, 37147−37161

Table 2. Optical Band Gaps for $BiVO_4$ and the $BiVO_4$/MWCNTs Nanocomposite

materials	wavelength (nm)	energy band gap (eV)
$BiVO_4$ nanostructures before adding MWCNTs	466	2.6
$BiVO_4$/MWCNTs nanocomposite	520	2.48

powders.[47−51] Besides, the pure $BiVO_4$ absorption edge shows a red shift. The band gap energy E_g value can be calculated using the Tauc plot of the $(\alpha h\upsilon)^2$ versus photon energy $(h\upsilon)$ curve with $n = 1/2$ for direct transition, as shown in the inset of Figure 2(b). The calculated band gap of $BiVO_4$ is $E_g = 2.6$ eV. In the case of the $BiVO_4$/MWCNTs nanocomposite, the absorbance of the $BiVO_4$/MWCNTs nanocomposite increased noticeably in the visible region at 520 nm after being synthesized at 180 °C for 12 h, as shown in Figure 3. The absorbance ability of $BiVO_4$/MWCNTs increases after the addition of a tiny amount of MWCNTs, as shown in Figure 3(a). The addition of MWCNTs results in a greater ability of absorption of the nanocomposite. As well as the interesting property of the $BiVO_4$/MWCNTs nanocomposite is a slight red shift compared with pure $BiVO_4$. The process of visible light absorption is the transition from the valence band (VB) to the V 3d conduction band (CB), which results in a slight red shift.[46] Additionally, compared to pure $BiVO_4$, it was clear from the inset of Figure 3(b) that the $BiVO_4$/MWCNTs nanocomposite exhibited the narrowest band gap energy of about $E_g = 2.48$ eV. The localized levels positioned between the valance band and the conduction band resulted in moving Fermi levels to the conduction band of the nanocomposite.

These findings are consistent with earlier research.[52,53] Additionally, lowering the band gap energy of nanocomposites is related to the effects of the quantum volume effect, which results in a reduction in the energy gap band and a shift in absorbance from the valence band to the conduction band[54] toward long wavelengths.

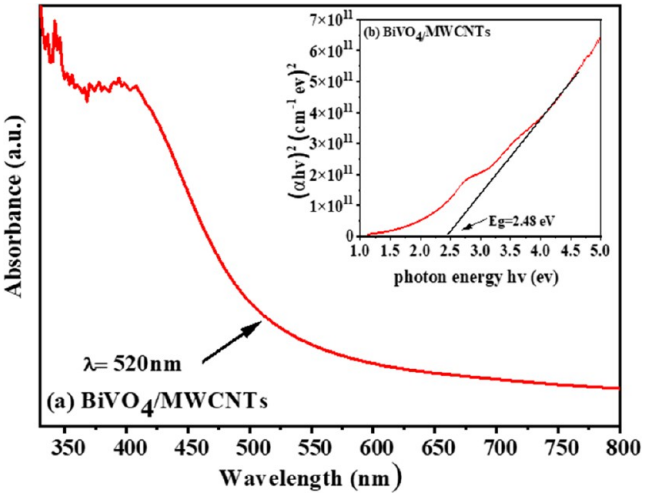

Figure 3. (a) Optical absorbance spectra and (b) calculated band gap E_g using the plot of the variation of $(\alpha h\upsilon)^2$ versus $(h\upsilon)$ of the $BiVO_4$/MWCNTs nanocomposite.

Raman spectroscopy is a suitable method for examining the local structure of materials.[55] In Figure 4(a,b), typical Raman spectra of pure $BiVO_4$ and the $BiVO_4$/MWCNTs nanocomposite were determined, respectively. As shown in pure $BiVO_4$, the symmetric V−O stretching vibration mode is given to the dominant peak at 800 cm^{-1} in Figure 4(a). However, the resulting sample from the hydrothermal method is attributed to an unremarkable peak at 708 cm^{-1}. The peak at 201 cm^{-1} was attributed to the external mode, whereas the peak at 323 cm^{-1} was related to the vanadate anion's antisymmetric bending mode, as shown in Table 3. The Raman peak of the $BiVO_4$/MWCNTs nanocomposite in Figure 4(b) indicates that the

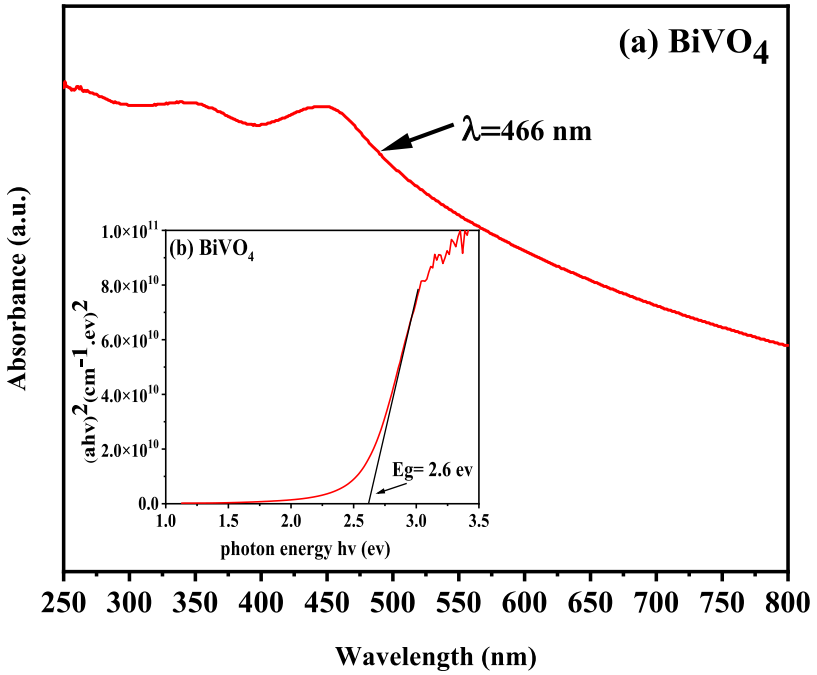

Figure 2. (a) Optical absorbance spectra and (b) calculated band gap E_g using the plot of the variation of $(\alpha h\upsilon)^2$ versus photon energy $(h\upsilon)$ of $BiVO_4$ nanostructures.

https://doi.org/10.1021/acsomega.3c04722
ACS Omega 2023, 8, 37147−37161

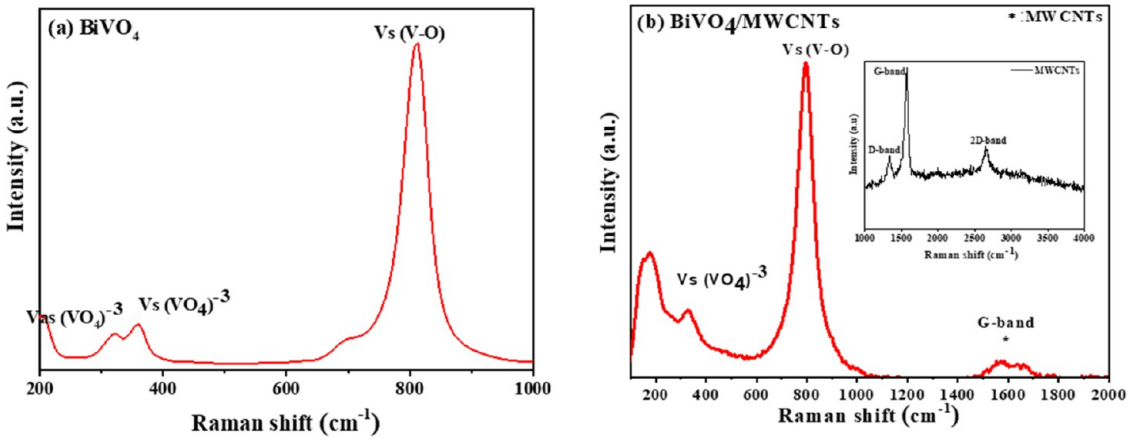

Figure 4. Raman spectra of (a) pure $BiVO_4$ and (b) $BiVO_4$/MWCNTs nanocomposite with the inset image of MWCNTs.

Table 3. Position and Assignation of Raman Bands for $BiVO_4$ and the $BiVO_4$/MWCNTs Nanocomposite Synthesized by the Hydrothermal Method

material	Raman bands (cm^{-1})	assignation
$BiVO_4$ nanostructure before adding MWCNTs	824	vs (V−O)
	378	vs VO_4^{-3}
	337	vas VO_4^{-3}
	213	external mode
	129	external mode
$BiVO_4$/MWCNTs nanocomposite	820	vs (V−O)
	362	vs VO_4^{-3}
	323	vas VO_4^{-3}
	206	external mode
	130	external mode
	1540	G-band of MWCNTs

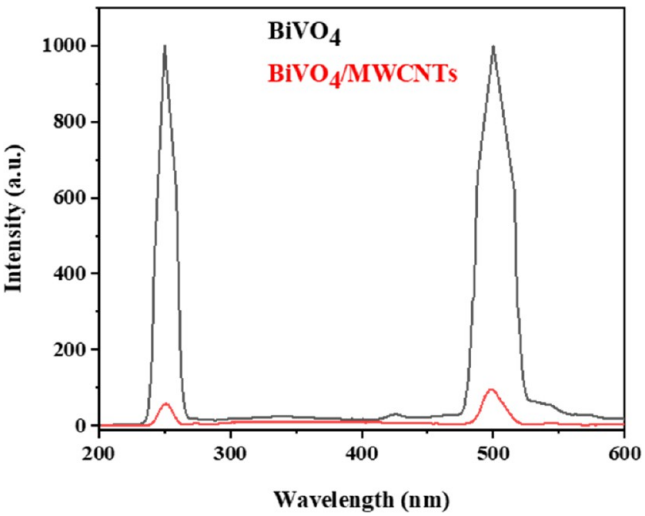

Figure 5. PL spectra of pure $BiVO_4$ (black line) and the $BiVO_4$/MWCNTs nanocomposite (red line).

presence of MWCNTs had no impact on the short-range symmetry of VO_4 tetrahedra, except for the characteristic peaks linked to $BiVO_4$.[56] Additionally, the peak at 1582 cm^{-1} was connected to the G-band of the order structures of MWCNTs, further confirming the inclusion and embedding of MWCNTs in the composite's exterior mode.[56,57] The Raman analysis of MWCNTs in the inset image of Figure 4(b) displays that the G-band is about 1571 cm^{-1}. This shift to a high value is related to the chemical oxidation of MWCNTs and $BiVO_4$ by the hydrothermal method.

The PL spectra of the resulting $BiVO_4$ and $BiVO_4$/MWCNTs nanocomposite samples were employed to verify the photo-induced charge recombination and electron migration, as shown in Figure 5. The PL spectrum of $BiVO_4$ (black line) is compared with that of the $BiVO_4$/MWCNTs (red line) nanocomposite under the excitation wavelength of 250 nm. It can be suggested that PL showed each sample had two relatively obvious peaks. PL measurement was carried out to investigate the effect of MWCNTs on the photocatalytic process. The addition of MWCNTs resulted in an increased amount of Bi^{5+}, V^{+5}, and surface-adsorbed oxygen species, in which all species enhanced the −OH generation and decreased the recombination rate of electron−hole pairs, as shown in Figure 5.[58] The weaker PL intensity in the $BiVO_4$/MWCNTs nanocomposite was related to lower recombination rate of the photogenerated (e−h) pairs. Thereby, the emission intensity of the $BiVO_4$/MWCNTs nanocomposite is lower than that of pure $BiVO_4$, which may be due to the existence of MWCNTs inhibiting the recombination of the photogenerated charges.[59]

The transmission electron microscopy images (TEM) were utilized to study the morphology and microstructure of pure $BiVO_4$ and the $BiVO_4$/MWCNTs nanocomposite, as demonstrated in Figures 6(a,b) and 7(a−d) at different magnifications, respectively. It can be seen from Figure 6(a,b) that the primary particles of pure $BiVO_4$ are made of nanoparticles that are presented as somewhat larger particles and aggregated to create a cluster with an average diameter of about 0.044 μm during the hydrothermal method. Moreover, the resulting $BiVO_4$ microsphere with irregular edges is built by many tiny nanoflakes, which were observed as smaller and more regular particles in a relatively large aggregate. The generated $BiVO_4$ nanostructures were first combined into building blocks and then self-assembled by the Ostwald ripening process.[60−62] Meanwhile, the structure of the synthesized $BiVO_4$/MWCNTs nanocomposite is observed in Figure 7(a−d) at different magnifications. It was found that MWCNTs embedded inside the structure of $BiVO_4$ nanoflakes form a ternary heterojunction of the $BiVO_4$/MWCNTs nanocomposite with an average grain size of 34.9. It is worth noting that the nanocomposite appeared to be significantly greater than pure $BiVO_4$, which is about 15.5 nm.

https://doi.org/10.1021/acsomega.3c04722
ACS Omega 2023, 8, 37147−37161

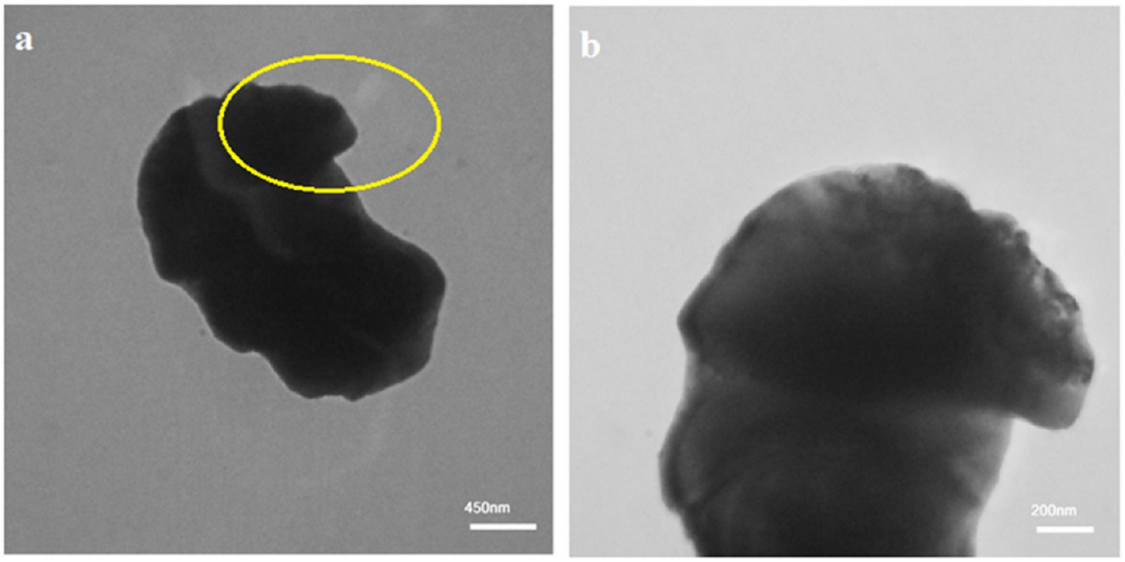

Figure 6. TEM images of the pure $BiVO_4$ nanostructures at different magnifications: (a) 450 and (b) 200 nm.

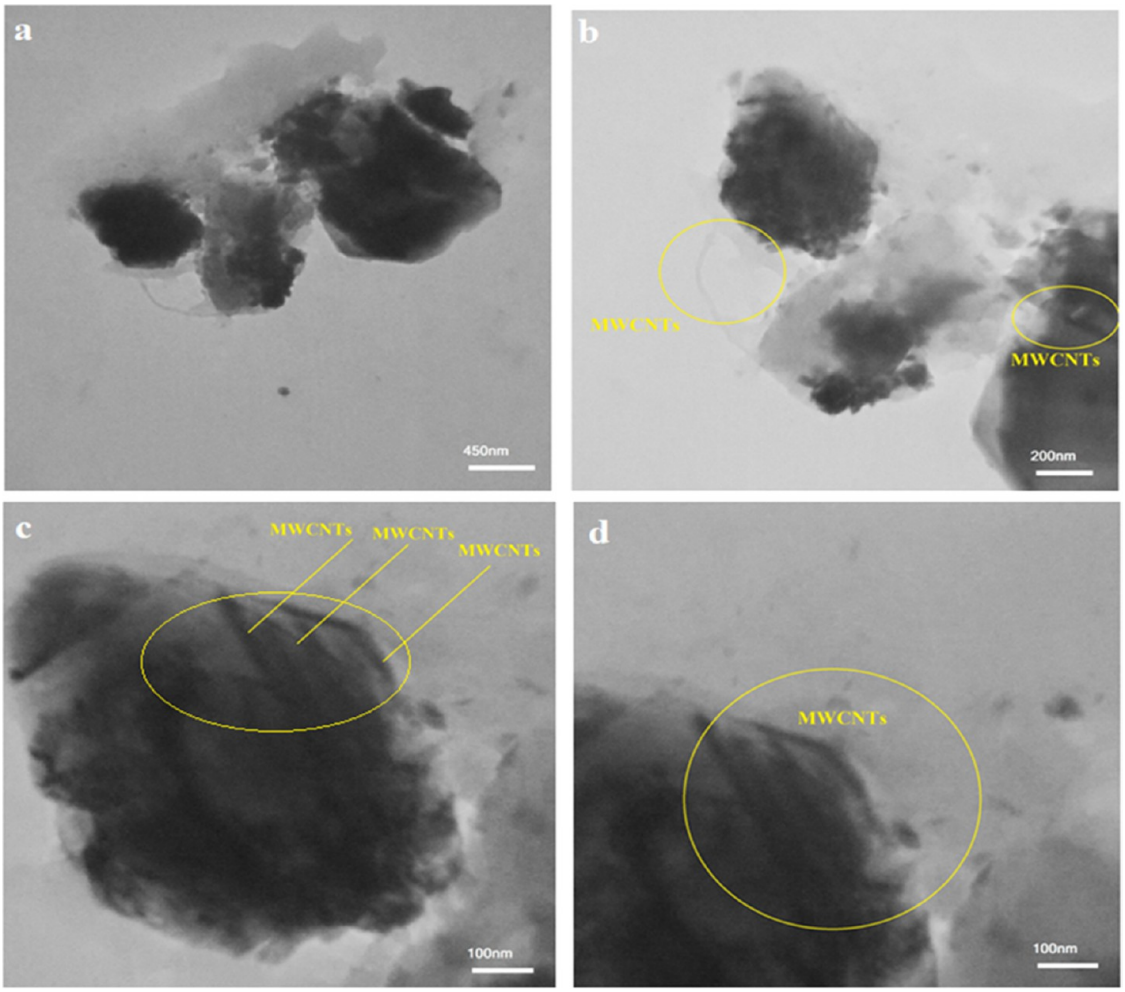

Figure 7. TEM images of the $BiVO_4$/MWCNTs nanocomposite at different magnifications: (a) 450, (b) 200, and (c, d) 100 nm.

These findings demonstrate that MWCNTs and $BiVO_4$ have been successfully coupled.[63−65]

In Figure 8 (right panel), the EDS spectrum indicates the $BiVO_4$ sample elemental analysis including Bi, V, and O. This result is consistent with the XRD analysis.[66] Besides, the EDS spectrum shows new strong signals of carbon such as Bi, V, O, and C, which belong to the $BiVO_4$/MWCNTs nanocomposite, as shown in Figure 8 (left panel). The 1:1 Bi/V atomic ratio is quite close to the value predicted by theory for $BiVO_4$. As stated

https://doi.org/10.1021/acsomega.3c04722
ACS Omega 2023, 8, 37147−37161

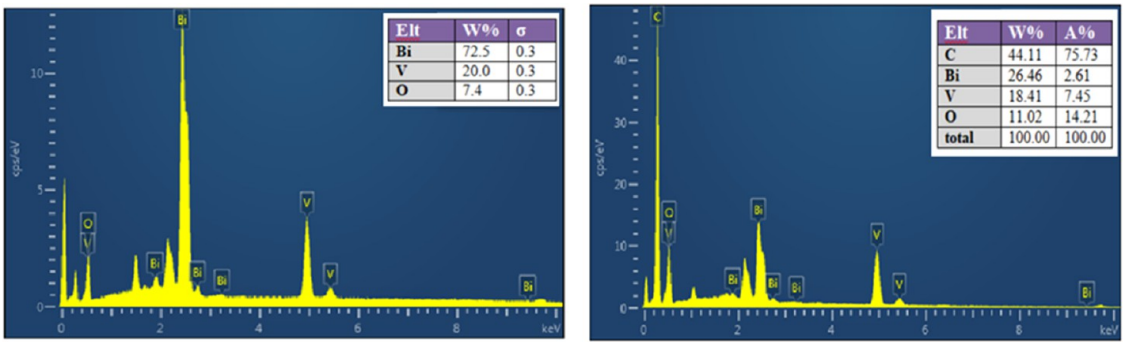

Figure 8. EDX spectrum of the pure $BiVO_4$ nanostructures (right panel) with an inset table and the $BiVO_4$/MWCNTs nanocomposite (left panel) with the inset table showing the percentage of each element in $BiVO_4$ and the $BiVO_4$/MWCNTs nanocomposite.

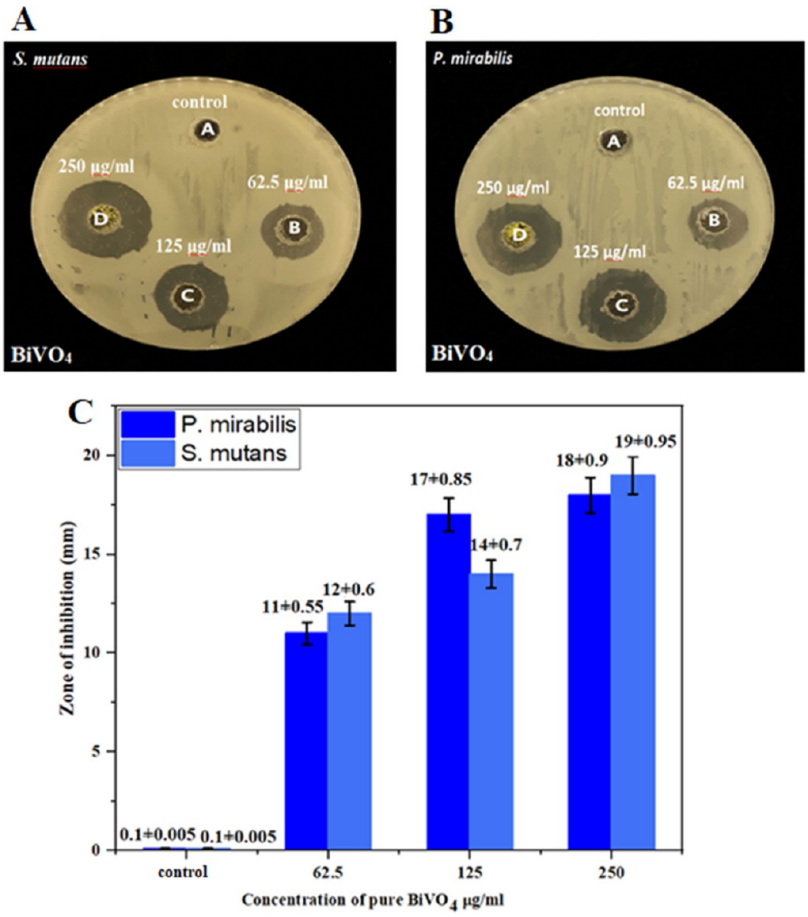

Figure 9. Antibacterial activity of the pure $BiVO_4$ nanostructure at different concentrations (26.5, 125, and 250 μg/mL) against (A) *P. mirabilis* and (B) *S.mutans*. (C) Data represented as the mean ± SD of three independent experiments.

in the literature,[63] some MWCNTs are implanted inside $BiVO_4$ and some are exposed on its surface.

3.2. Antibacterial Activity of Pure $BiVO_4$ and the $BiVO_4$/MWCNTs Nanocomposite. The antibacterial activity of the pure $BiVO_4$ nanostructure against *P. mirabilis* and *S. mutans* bacterial strains was evaluated at different concentrations of 26.5, 125, and 250 μg/mL. As shown in Figure 9(A–C), the pure $BiVO_4$ nanostructure demonstrated a strong antibacterial effect against both bacterial strains. The inhibition zones at high concentrations were about 12 ± 0.6, 14 ± 0.7, and 19 ± 0.9 mm against *S. mutans* and about 11 ± 0.5, 17 ± 0.8, and 18 ± 0.9 mm against *P. mirabilis* a in Figure 9(A,B), respectively. It was also found that the inhibitory effect of pure $BiVO_4$ increased as the concentration increased, especially at 125 and 250 μg/mL with IZ of about 18 and 17 mm in *P. mirabilis*, as shown in Figure 9(C) using data as mean ± SD of three independent tests. Our finding demonstrated that the antibacterial properties of the nanostructures are influenced by their size, surface morphology, and bacterial strains.

The outcomes also reveal that the antibacterial effects of $BiVO_4$ increased related to an increase in the bacterial membrane permeability for the entry of $BiVO_4$ nanostructure shape with an abrasive texture, which causes membrane disorganization and alterations at the protein level. This ultimately causes cellular metabolism to be inhibited, which results in bacterial cell death. Besides, the hydrothermal

https://doi.org/10.1021/acsomega.3c04722
ACS Omega 2023, 8, 37147−37161

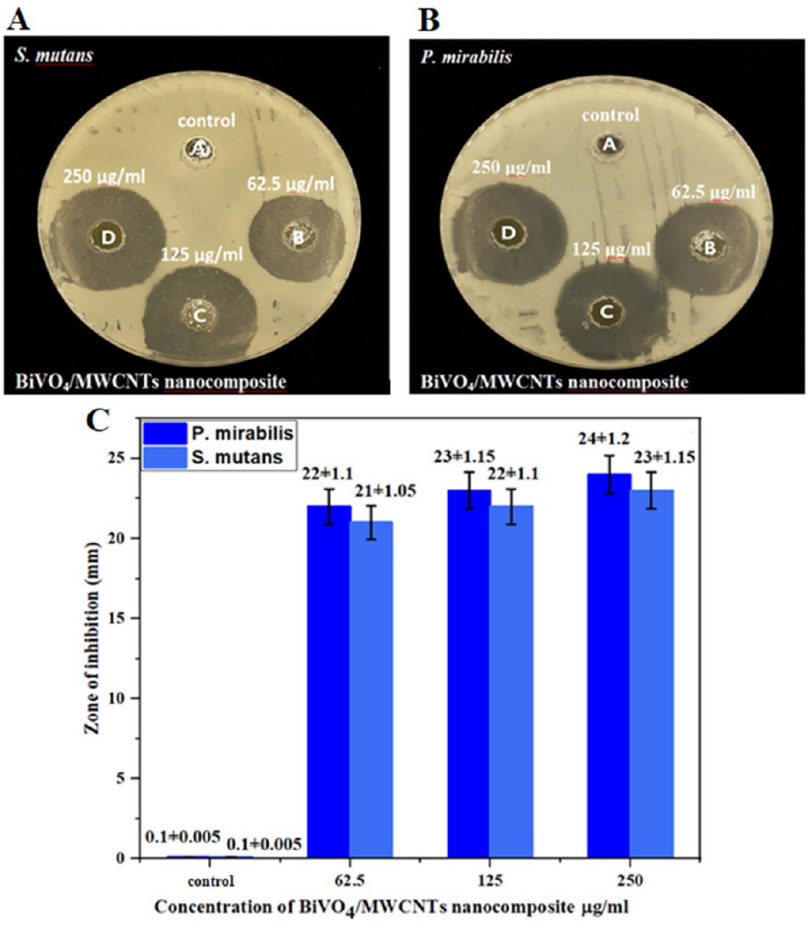

Figure 10. Antibacterial activity of the $BiVO_4$/MWCNTs nanocomposite at different concentrations (26.5, 125, and 250 μg/mL) against (A) *P. mirabilis* and (B) *S.mutans*. (C) Data represented as mean ± SD of three independent experiments.

synthesis resulted in a crystalline monoclinic structure nanostructure that offers high surface area and monodispersion evident from XRD analysis, which further contributes to the inactivation of bacteria.[67,68] Figure 10(A–C) illustrates the antibacterial effect of the synthesized $BiVO_4$/MWCNTs nanocomposite at various concentrations (26.5, 125, and 250 μg/mL) against *P. mirabilis* and *S. mutans* bacteria using the agar well diffusion assay. The results in Figure 10(A,B) exhibited that the tested bacterial strain, *P. mirabilis,* was highly susceptible bacteria, revealing a large inhibition zone of about 22 ± 1.1, 23 ± 1.1, and 24 ± 1.2 mm, while *S. mutans* became less susceptible bacteria, revealing an inhibition zone of about 21 ± 1.0, 22 ± 1.1, and 23 ± 1.1 mm with increasing concentrations. Based on the results of mean ± standard deviation obtained in Figure 10(C), it was clear that the $BiVO_4$/MWCNTs nanocomposite had superior antibacterial action against *P. mirabilis* bacteria to *S. mutans* bacteria. This might be due to differences in metabolism and cell physiology as well as the peptidoglycan (PG) layer of *P. mirabilis* being thinner than that of *S. mutans*.[69−71] Additionally, MWCNTs are the sites where $BiVO_4$ ions are stored after they are released from the $BiVO_4$ oxide nanostructure and come into contact with harmful bacteria. This increases cell permeability, which in turn leads to cell deformation and leakage. In general, nanocomposites having a high surface-to-volume ratio, which boosts the number of ions released from the nanostructure, performed better against bacteria.[72] In addition to the direct effect of the $BiVO_4$ nanostructure, the antibacterial activity of the nanocomposites is also improved by accelerating the diffusion of Bi^{3+} ions into VO_4^{-3} anions,[73,74] which supports the thermodynamic nucleation and the production of reactive oxygen species (ROS). In general, pathogenic bacteria's intercellular or cell walls undergo a complicated response as part of the nanostructures' antibacterial mechanism,[75] first distortion and then a leak. In general, nanocomposites having a high surface-to-volume ratio, which boosts the number of ions released from the nanostructure, performed better against bacteria.[76] MIC values of pure $BiVO_4$ and the $BiVO_4$/MWCNTs nanocomposite against *S. mutans* and *P. mirabilis* have been measured. The MIC of pure $BiVO_4$ is 31.232 μg/mL for both bacterial strains, while that of $BiVO_4$/MWCNTs is 15.616 μg/mL.

As shown in Figure 11(A–C), the SEM morphology indicates the visualization of the effect of pure $BiVO_4$ and the $BiVO_4$/MWCNTs nanocomposite on the cellular morphology to observe the membrane of cytoplasm deformation of *S. mutans* and *P. mirabilis* upon being treated. As shown in Figure 11(A), both untreated bacterial strains reveal normal shapes and sizes of bacteria. Besides, the bacterial strains showed changes in the cell membranes like damaged, blabbed, and clumped membranes. The morphology of *P. mirabilis* (Gram −ve) indicates that they exist as single-celled or rod-shaped. Whereas *S. mutans* (Gram +ve) has a coccus shape that usually occurs in clusters but also can be observed in single and pair cells in an untreated state. As shown in Figure 11(B,C), the morphology of *P. mirabilis* and *S. mutans* after being exposed to $BiVO_4$ and the $BiVO_4$/MWCNTs nanocomposite displays that some of the cells have changed.

https://doi.org/10.1021/acsomega.3c04722
ACS Omega 2023, 8, 37147−37161

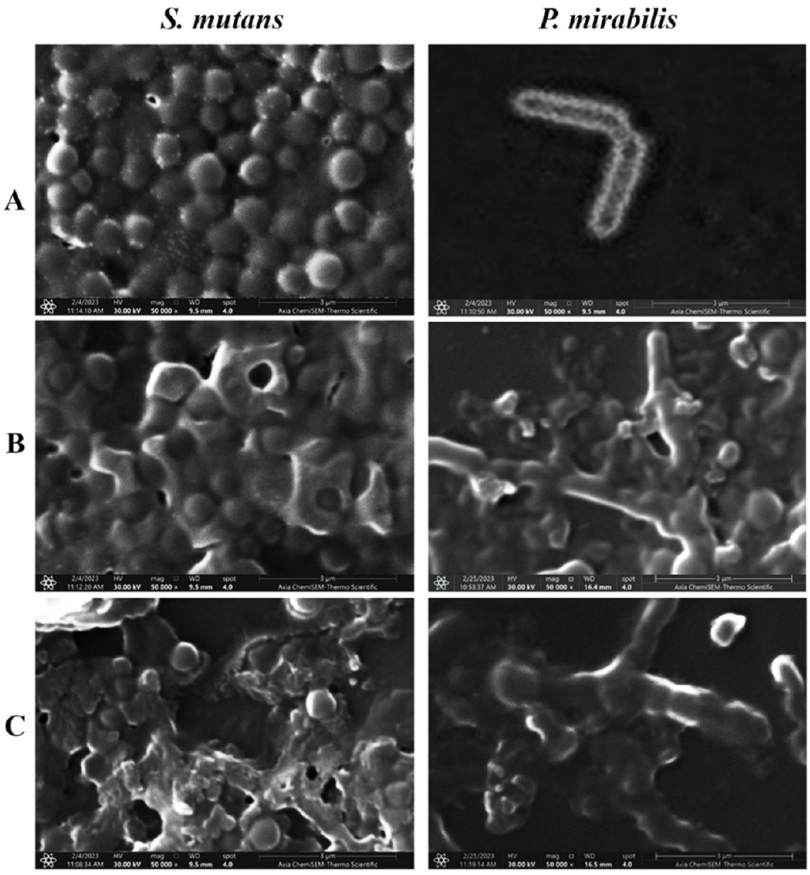

Figure 11. SEM morphology visualized the effect of pure $BiVO_4$ and the $BiVO_4$/MWCNTs nanocomposite on the cytoplasm deformation and alterations in the cell membranes like damaged, blabbed, and clumped *S. mutans* and *P. mirabilis*. (A) Untreated control bacterial strains. (B) Bacterial strains treated with pure $BiVO_4$. (C) Bacterial strains treated with $BiVO_4$ /MWCNTs.

Besides, aggregation with bacteria cell membranes is common in many types of carbon-based nanoparticles. Moreover, after being treated with the $BiVO_4$ /MWCNTs nanocomposite, the damaged membrane caused the loss of cytoplasmic components, which resulted in cell death. These created nanocomposites were extremely effective in killing both Gram +ve and Gram −ve bacteria due to the synergistic effects of the inherent multimodal killing mechanism of nanoparticles and the cell-penetrating capacity of MWCNTs.

According to the findings, the mechanism of nanostructures that inhibits bacteria in this way is accomplished by (i) damaging the bacterial cell wall, (ii) interfering with DNA replication and the production of reactive oxygen species (ROS), (iii) inhibiting protein synthesis, and (iv) interfering with the bacterium's metabolism, as shown in Figure 11(A−C).[77] The most crucial factors in determining whether pathogenic bacteria are inhibited are the magnitude and production of ROS (h^+, $^\bullet O_2^-$, and OH−). Since ROS can cause oxidation of proteins and peroxidation of lipids, which changes the permeability of fluids and ion transport and damages the hardness of cell membranes, ROS can also hinder metabolic activities.[78] A study by Ye et al.[79] demonstrated that the MWCNT/$BiVO_4$ nanocomposite plays a potential role as a therapeutic agent against multiple antibiotic resistance, *Shigella flexneri* HL, which is present in livestock and poultry breeding wastewater. A study by ref 80 represented that $BiVO_4$@ACFs under different chelating agents showed highly antibacterial activity against *Escherichia coli* and *Staphylococcus aureus*. In the study of ref 81, the activity of different MO (Ag_2O_x, CoO_x, and CuO_x) and different wt % loadings of CuO_x in $MoBiVO_4$ photocatalysts on photocatalytic inactivation and degradation of orange II dye in visible light irradiation was investigated. The CuO_x loading significantly enhanced the photocatalytic degradation activity of Mo−$BiVO_4$ photocatalysts for bacteria and orange II dye because of the appropriate charge separation and transfer at the Mo−$BiVO_4$ interface. The optimum CuO_x (2 wt %)/Mo−$BiVO_4$ photocatalysts prepared using the wet impregnation method exhibited the maximum inactivation efficiency (98%) for *E. coli* and *S. aureus* over 120 min. Moreover, the optimized CuO_x (2 wt %)/Mo−BiVO4 photocatalysts showed outstanding inactivation of *E. coli* and *S. aureus* (98%) compared to the other prepared photocatalysts. Taken together, the results of the current study confirmed that the $BiVO_4$/MWCNTs nanocomposite has significantly enhanced antibacterial activity as compared to $BiVO_4$ alone. The antibacterial activity of the $BiVO_4$/MWCNTs nanocomposite could lead to ROS generation, which disrupts the plasma membrane and destroys metabolic pathways, leading to bacterial cell death. Consequently, we offer a novel antibacterial approach for future disinfection applications.

3.3. Inhibition of Biofilm Formation. Figure 12 exhibits the ability of pure $BiVO_4$ and the $BiVO_4$/MWCNTs nanocomposite to inhibit biofilm formation for both *P. mirabilis* and *S. mutans*. Biofilm formation represented an important step in the initiation of any infection. The adhesion of bacterial strains to a surface is an essential first step in biofilm formation and can occur through specific and nonspecific cell−surface interactions. These biofilms can be detected by staining the adhered bacterial

https://doi.org/10.1021/acsomega.3c04722
ACS Omega 2023, 8, 37147−37161

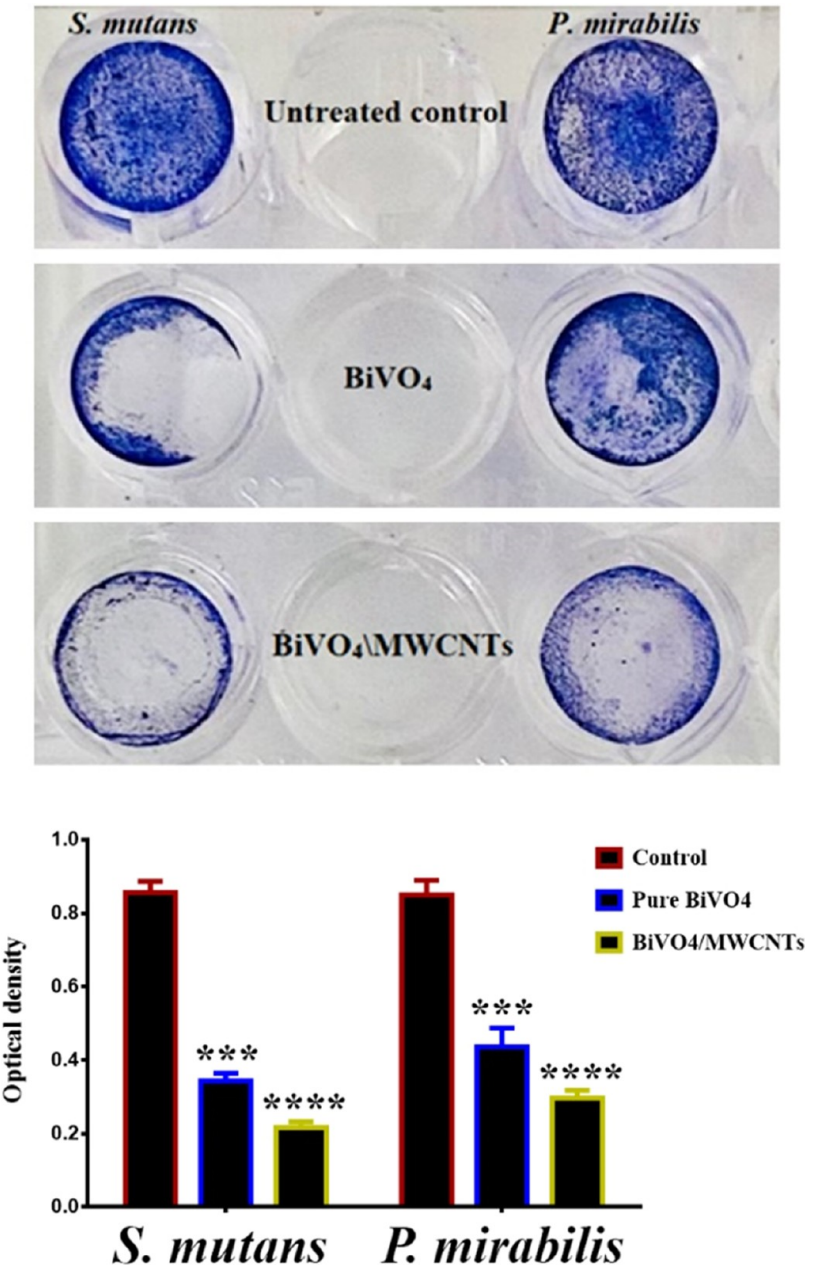

Figure 12. Pure $BiVO_4$ and $BiVO_4$/MWCNTs reduce biofilm formation in bacterial strains (upper panel). The bottom panel represents the quantification of biofilm formation as determined by crystal violet staining. Data are represented as the mean ± SD of three independent experiments.

cells with crystal violet. In this test, the effect of pure $BiVO_4$ and $BiVO_4$/MWCNTs in inhibiting biofilm formation was demonstrated, as shown in Figure 12 (upper panel). Besides, pure $BiVO_4$ and $BiVO_4$/MWCNTs showed high effectiveness in biofilm formation (lower panel). The results showed that pure $BiVO_4$ and $BiVO_4$/MWCNTs significantly impaired the growth of microbial strains. These reductions in biofilm formation could be related to the mechanism of reactive oxygen species (ROS) formation. These ROS can result in the oxidation of proteins and the peroxidation of lipids, which weaken the Gram +ve cell membrane, alter the permeability of fluids and ion transport, and prevent metabolic processes from occurring.[82] In addition, the interactions between the cell and the NPs, whether electrostatic or direct, can cause harm to the outer membrane of Gram +ve and Gram −ve bacteria's cell walls.

Our results suggest that nanotechnology has potential applications as an antibacterial agent during bacterial infections.[83] The nanotechnology approved its potential applications as antiparasitic agents.[84−86] Additionally, nanoparticles are used widely in fish[87,88] and poultry[89] production.

3.4. Role of $BiVO_4$ and $BiVO_4$/MWCNTs in Bacterial Biofilm Inhibition. To study the effect of pure $BiVO_4$ and the $BiVO_4$/MWCNTs nanocomposite on bacterial biofilm inhibition, confocal microscopy was used. The confocal results confirmed the antibiofilm effects of pure $BiVO_4$ and the $BiVO_4$/MWCNTs nanocomposite at a concentration of 125 μg/mL. The biofilm viability kit provides a two-color fluorescence stain and is used to distinguish between live and dead bacterial cells within the biofilm community based on membrane integrity. As shown in Figure 13(A−C), the Syto 9 green fluorescence dye stained healthy membranes, whereas propidium iodide red

https://doi.org/10.1021/acsomega.3c04722
ACS Omega 2023, 8, 37147−37161

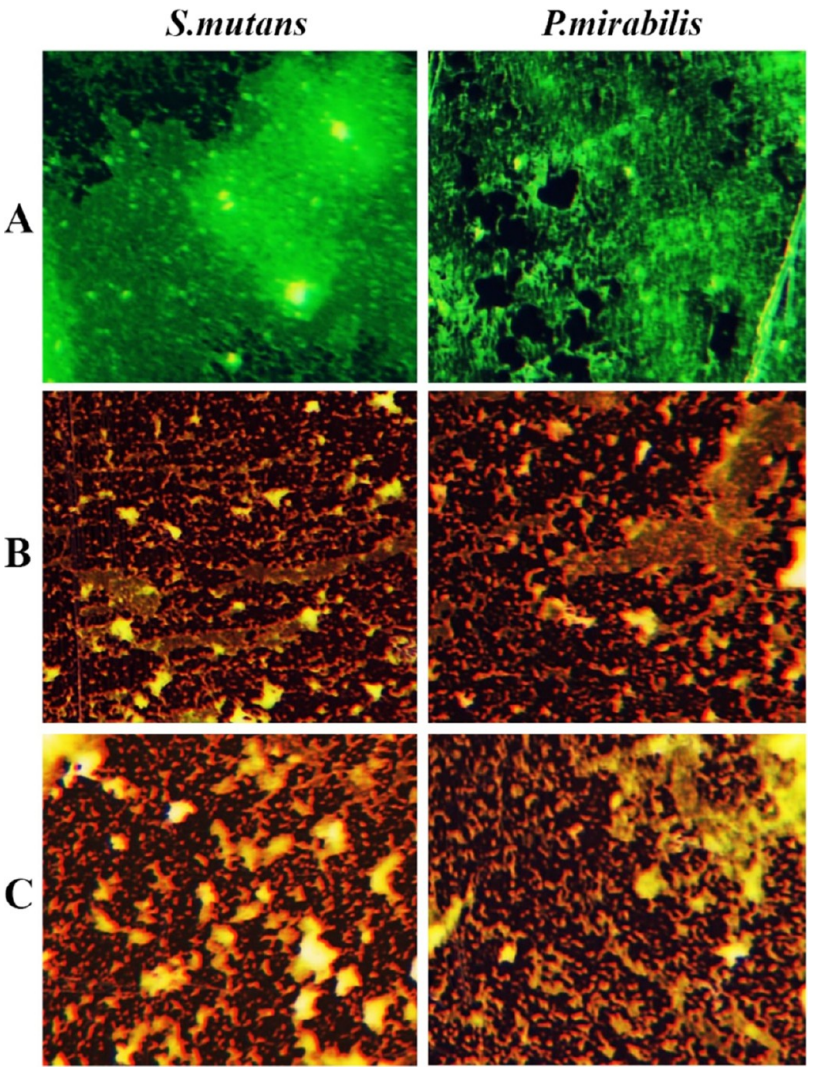

Figure 13. Reduction of the level of bacterial biofilm formation. Untreated control bacterial strains (A). Bacterial strains were treated with pure $BiVO_4$ (B). Bacterial strains were treated with $BiVO_4$/MWCNTs (C).

fluorescence dye penetrated and stained the bacterial strains with damaged membranes; bacteria with intact cell membranes were stained fluorescent green, whereas bacteria with damaged membranes were stained fluorescent red, as indicated in Figure 13(A). The control of untreated biofilm bacterial strains showed green fluorescence, whereas the biofilm of treated samples and the cells of the treated bacterial strain exhibited orange to red fluorescence; these results demonstrated the presence of dead bacterial strains after being treated with pure $BiVO_4$ and the $BiVO_4$/MWCNTs nanocomposite at a concentration of 125 μg/mL. The control untreated bacterial strains were aggregated and covered with a mature biofilm structure, while the bacterial strains that were treated with pure $BiVO_4$ and the $BiVO_4$/MWCNTs nanocomposite at a concentration of 125 μg/mL were less aggregated and had a less dense biofilm covering, as shown in Figure 13(B,C). Taken together, the results of the current study reveal the potential biofilm formation inhibition and effects of pure $BiVO_4$ and the $BiVO_4$/MWCNTs nanocomposite. The biofilm metabolic activity of *S. mutans* and *P. mirabilis* was investigated using a flow cytometry assay.

Figure 14 shows the dot plots of the *S. mutans* and *P. mirabilis* biofilm evaluated by flow cytometry. This assay used to measure metabolic activity in the *S. mutans* and *P. mirabilis* biofilm generated for 48 h assisted the distinction between live and dead cell populations done with excitation/emission fluorescence Syto 9 and propidium iodide stains. In the control untreated bacterial strain, as shown in Figure 14 (upper panel), the percentage of live *S. mutans* was 83.13%, while that of *P. mirabilis* was 80.66% after being treated with pure $BiVO_4$ and the $BiVO_4$/MWCNTs nanocomposite at a concentration of 125 μg/mL. These percentages decreased to 10.44 and 5.41%, respectively, when the bacterial strain was treated with pure $BiVO_4$, as shown in Figure 14 (middle panel). The percentages of live cells were 1.95 and 1.20%, respectively, when bacterial strains were treated with the $BiVO_4$/MWCNTs nanocomposite, as indicated in Figure 14 (lower panel). The $BiVO_4$/MWCNTs nanocomposite had a higher effect than pure $BiVO_4$ in the reduction of live cells.

4. CONCLUSIONS

In this study, $BiVO_4$ and $BiVO_4$/MWCNTs nanocomposites were prepared by using the hydrothermal method. The prepared materials were analyzed by using different characterization methods, which indicated that the introduction of a small number of MWCNTs does not affect the $BiVO_4$ monoclinic structure, as revealed in XRD analysis. Additionally, related to

https://doi.org/10.1021/acsomega.3c04722
ACS Omega 2023, 8, 37147−37161

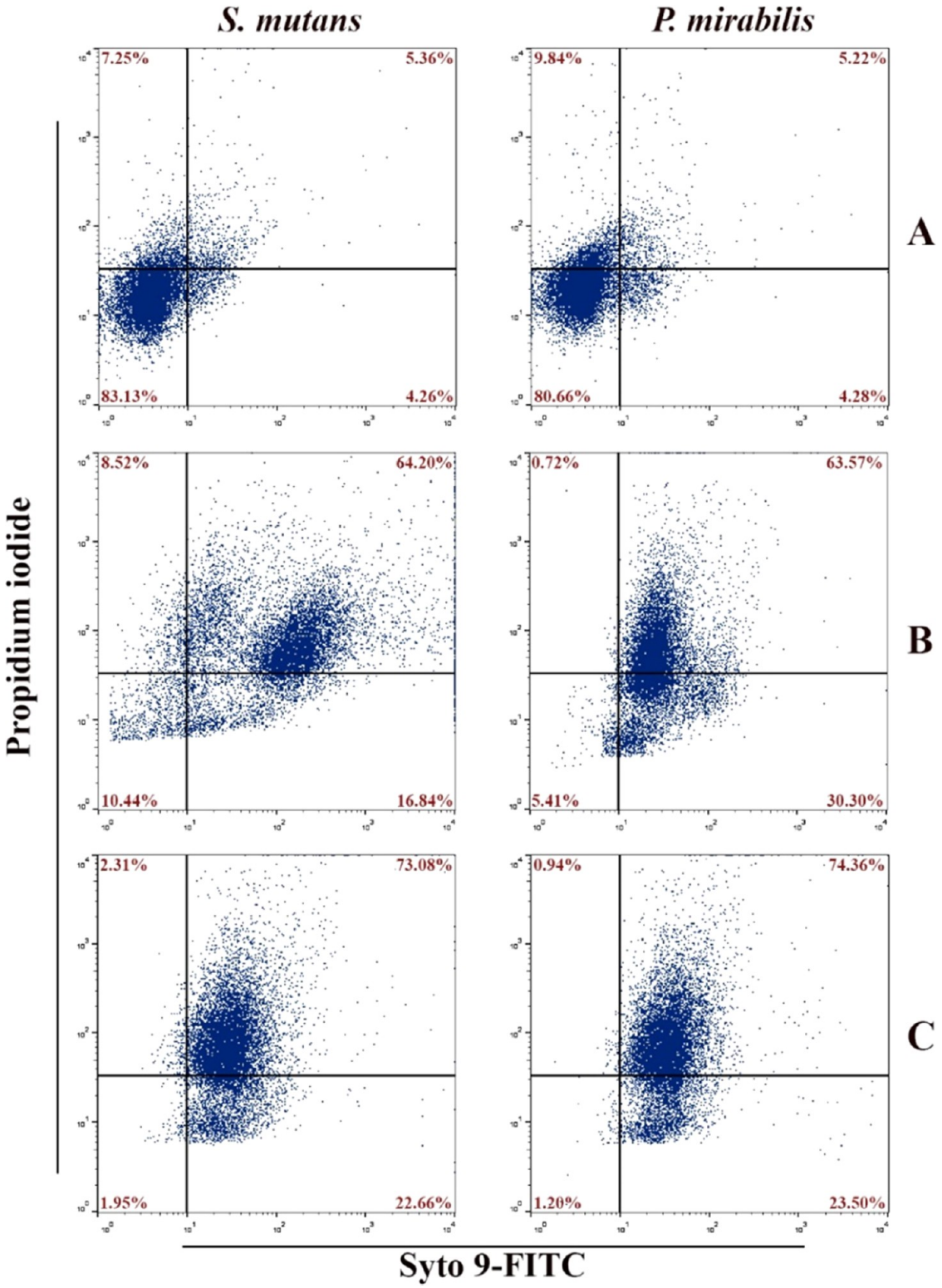

Figure 14. Effect of pure $BiVO_4$ and $BiVO_4$/MWCNTs on metabolic activity in the *S. mutans* and *P. mirabilis* biofilm. (A) Control untreated bacterial strains (upper panel), (B) bacterial strains treated with pure $BiVO_4$ (middle panel), and (C) bacterial strains treated with $BiVO_4$/MWCNTs (lower panel).

the embedding of MWCNTs in $BiVO_4$, the visible light absorption range shifts to the red region because of the localized levels positioned between the valence band and the conduction band, resulting in a reduction in the energy gap band, as shown in the UV−visible spectrum. The PL spectrum of the $BiVO_4$/MWCNTs nanocomposite improved the separation of carriers considerably, which resulted in the creation of more active sites and increasing adsorption capacity. Both pure $BiVO_4$ and $BiVO_4$/MWCNTs exhibited promising antibacterial activity against tested bacterial strains and biofilm formation. Generally, the results of this study indicated that $BiVO_4$ and $BiVO_4$/MWCNTs nanocomposites significantly reduced bacterial

https://doi.org/10.1021/acsomega.3c04722
ACS Omega 2023, 8, 37147−37161

biofilm formation. Furthermore, these results suggest that $BiVO_4$ and $BiVO_4$/MWCNTs nanocomposites could be promising materials for developing antimicrobial agents.

AUTHOR INFORMATION

Corresponding Authors

Duha S. Ahmed − *Applied Sciences Department, University of Technology, Baghdad 11231, Iraq*; Email: Duha.S.Ahmed@uotechnology.edu.iq

Majid S. Jabir − *Applied Sciences Department, University of Technology, Baghdad 11231, Iraq*; orcid.org/0000-0003-0759-8298; Email: 100131@uotechnology.edu.iq

Ayman A. Swelum − *Department of Animal Production, College of Food and Agriculture Science, King Saud University, Riyadh 11451, Saudi Arabia*; orcid.org/0000-0003-3247-5898; Email: aswelum@ksu.edu.sa

Authors

Zeena R. Rhoomi − *Applied Sciences Department, University of Technology, Baghdad 11231, Iraq*

Balamuralikrishnan Balasubramanian − *Department of Food Science and Biotechnology, College of Life Science, Sejong University, Seoul 05006, Republic of Korea*

Maged A. Al-Garadi − *Department of Animal Production, College of Food and Agriculture Science, King Saud University, Riyadh 11451, Saudi Arabia*

Complete contact information is available at: https://pubs.acs.org/10.1021/acsomega.3c04722

Author Contributions

Conceptualization: Z.R.R., D.S.A., and M.S.J.; methodology: Z.R.R., D.S.A., and M.S.J.; software: B.B., M.A.A.-G., and A.A.S.; validation: B.B., M.A.A.-G., and A.A.S.; formal analysis: M.A.J.; investigation: Z.R.R., D.S.A., and M.S.J.; resources: M.S.J.; data curation: D.S.A.; writing original draft preparation: Z.R.R., D.S.A., and M.S.J.; writing—review and editing: D.S.A., M.S.J., B.B., M.A.A.-G., and A.A.S.; visualization: B.B., M.A.A.-G., and A.A.S.; supervision: D.S.A. and M.S.J.; and project administration: D.S.A. and M.S.J. All authors have read and agreed to the published version of the manuscript.

Funding

The authors extend their appreciation to the Researchers Supporting Project Number (RSPD2023R971), King Saud University, Riyadh, Saudi Arabia, for funding this research.

Notes

The authors declare no competing financial interest.

Institutional Review Board Statement The study was conducted according to the guidelines of the Declaration of Helsinki and approved by the Institutional Review Board of the University of Technology, Baghdad, Iraq (ref no. DAS 23−9−2021).

ACKNOWLEDGMENTS

The authors extend their appreciation to the Researchers Supporting Project Number (RSPD2023R971), King Saud University, Riyadh, Saudi Arabia, for funding this research. The authors appreciated the University of Technology, Iraq, for their support.

REFERENCES

(1) Duan, H.; Wang, D.; Li, Y. Green chemistry for nanoparticle synthesis. *Chem. Soc. Rev.* **2015**, *44* (16), 5778−5792.

(2) Yang, H. G.; Liu, G.; Qiao, S. Z.; et al. Solvothermal synthesis and photoreactivity of anatase TiO_2 nanosheets with dominant {001} facets. *J. Am. Chem. Soc.* **2009**, *131* (11), 4078−4083.

(3) Jun, Y. W.; Choi, J. S.; Cheon, J. Shape control of semiconductor and metal oxide nanocrystals through nonhydrolytic colloidal routes. *Angew. Chem., Int. Ed.* **2006**, *45* (21), 3414−3439.

(4) Sinclair, T. S.; Hunter, B. M.; Winkler, J. R.; Gray, H. B.; Müller, A. M. Factors affecting bismuth vanadate photoelectrochemical performance. *Mater. Horiz.* **2015**, *2* (3), 330−337.

(5) Pandey, M.; et al. Targeted specific inhibition of bacterial and Candida species by mesoporous Ag/Sn−SnO_2 composite nanoparticles: in silico and in vitro investigation. *RSC Adv.* **2022**, *12* (2), 1105−1120.

(6) Roy, K.; Poompiew, N.; Pongwisuthiruchte, A.; Potiyaraj, P. Application of different vegetable oils as processing aids in industrial rubber composites: A sustainable approach. *ACS Omega* **2021**, *6* (47), 31384−31389.

(7) Guan, D.-L.; Niu, C.-G.; Wen, X.-J.; Guo, H.; Deng, C.-H.; Zeng, G.-M. Enhanced *Escherichia coli* inactivation and oxytetracycline hydrochloride degradation by a Z-scheme silver iodide decorated bismuth vanadate nanocomposite under visible light irradiation. *J. Colloid Interface Sci.* **2018**, *512*, 272−281.

(8) Sharma, R.; Singh, S.; Verma, A.; Khanuja, M. Visible light-induced bactericidal and photocatalytic activity of hydrothermally synthesized $BiVO_4$ nano-octahedrals. *J. Photochem. Photobiol., B* **2016**, *162*, 266−272.

(9) Regmi, C.; Kshetri, Y. K.; Jeong, S. H.; Lee, S. W. $BiVO_4$ as highly efficient host for near-infrared to visible upconversion. *J. Appl. Phys.* **2019**, *125* (4), No. 043101.

(10) Antuch, M.; Millet, P.; Iwase, A.; Kudo, A. The role of surface states during photocurrent switching: Intensity modulated photocurrent spectroscopy analysis of $BiVO_4$ photoelectrodes. *Appl. Catal., B* **2018**, *237*, 401−408.

(11) Kudo, A.; Omori, K.; Kato, H. A novel aqueous process for preparation of crystal form-controlled and highly crystalline $BiVO_4$ powder from layered vanadates at room temperature and its photocatalytic and photophysical properties. *J. Am. Chem. Soc.* **1999**, *121* (49), 11459−11467.

(12) Zhao, Y.; Xie, Y.; Zhu, X.; Yan, S.; Wang, S. Surfactant-free synthesis of hyperbranched monoclinic bismuth vanadate and its applications in photocatalysis, gas sensing, and lithium-ion batteries. *Chem. - Eur. J.* **2008**, *14* (5), 1601−1606.

(13) Marzano, I. M.; Franco, M.; Silva, P.; et al. Crystal structure, antibacterial and cytotoxic activities of a new complex of bismuth (III) with sulfapyridine. *Molecules* **2013**, *18* (2), 1464−1476.

(14) Abid, H. N.; Ahmed, D. S.; Al-keisy, A. H. Constructed p-2D/n-2D BiOCl/$BiVO_4$ Nanoheterostructure for Photocatalytic Antibacterial Activity. *ECS Trans.* **2022**, *107* (1), 2283.

(15) Noor, M.et al. *Effect of pH Variation on Structural, Optical and Shape Morphology of $BiVO_4$ Photocatalysts*, 10th International Conference on Electrical and Computer Engineering (ICECE); IEEE, 2018; pp 81−84.

(16) Rahman, M. F.; Haque, M.; Hasan, M.; Hakim, M. Fabrication of Bismuth Vanadate ($BiVO_4$) nanoparticles by a facile route. *Trans. Electr. Electron. Mater.* **2019**, *20* (6), 522−529.

(17) Zhao, H.; Tian, F.; Wang, R.; Chen, R. A review on bismuth-related nanomaterials for photocatalysis. *Rev. Adv. Sci. Eng.* **2014**, *3* (1), 3−27.

(18) Han, M.; Chen, X.; Sun, T.; Tan, O. K.; Tse, M. S. Synthesis of mono-dispersed m-$BiVO_4$ octahedral nano-crystals with enhanced visible light photocatalytic properties. *CrystEngComm* **2011**, *13* (22), 6674−6679.

(19) Madhusudan, P.; Yu, J.; Wang, W.; Cheng, B.; Liu, G. Facile synthesis of novel hierarchical graphene−$Bi_2O_2CO_3$ composites with enhanced photocatalytic performance under visible light. *Dalton Trans.* **2012**, *41* (47), 14345−14353.

(20) He, N.; Li, X.; Feng, D.; et al. Exploring the toxicity of a bismuth−asparagine coordination polymer on the early development of zebrafish embryos. *Chem. Res. Toxicol.* **2013**, *26* (1), 89−95.

(21) Sharifi, E.; Salimi, A.; Shams, E.; Noorbakhsh, A.; Amini, M. K. Shape-dependent electron transfer kinetics and catalytic activity of NiO nanoparticles immobilized onto DNA modified electrode: fabrication of highly sensitive enzymeless glucose sensor. *Biosens. Bioelectron.* **2014**, *56*, 313−319.
(22) Rocha, G.; Melo, L.; Castro, M., Jr; Ayala, A.; de Menezes, A.; Fechine, P. Structural characterization of bismuth rare earth tungstates obtained by fast microwave-assisted solid-state synthesis. *Mater. Chem. Phys.* **2013**, *139* (2−3), 494−499.
(23) Li, H.; Li, K.; Wang, H. Hydrothermal synthesis and photocatalytic properties of bismuth molybdate materials. *Mater. Chem. Phys.* **2009**, *116* (1), 134−142.
(24) Ahmed, D. S.; Mohammed, M. K.; Mohammad, M. R. Sol−gel synthesis of Ag-doped titania-coated carbon nanotubes and study their biomedical applications. *Chem. Pap.* **2020**, *74* (1), 197−208.
(25) Cioffi, C.; Campidelli, S.; Sooambar, C.; et al. Synthesis, characterization, and photoinduced electron transfer in functionalized single wall carbon nanohorns. *J. Am. Chem. Soc.* **2007**, *129* (13), 3938−3945.
(26) Eder, D. Carbon nanotube− inorganic hybrids. *Chem. Rev.* **2010**, *110* (3), 1348−1385.
(27) Heydari-Bafrooei, E.; Askari, S. Electrocatalytic activity of MWCNTs supported Pd nanoparticles and MoS_2 nanoflowers for hydrogen evolution from acidic media. *Int. J. Hydrogen Energy* **2017**, *42* (5), 2961−2969.
(28) Heydari-Bafrooei, E.; Shamszadeh, N. S. Synergetic effect of CoNPs and graphene as cocatalysts for enhanced electrocatalytic hydrogen evolution activity of MoS_2. *RSC Adv.* **2016**, *6* (98), 95979−95986.
(29) Mohammad, M. R.; Ahmed, D. S.; Mohammed, M. K. Synthesis of Ag-doped TiO_2 nanoparticles coated with carbon nanotubes by the sol−gel method and their antibacterial activities. *J. Sol−Gel Sci. Technol.* **2019**, *90* (3), 498−509.
(30) Mohammed, M. K.; Taqi, Z. J.; Hassen, A. M. A.; Jabir, M. S.; Ahmed, D. S. *SWCNTs/ZnO-Ag/ZnO-Au Nanocomposite Increases Bactericidal Activity of Phagocytic Cells against Staphylococcus aureus*, AIP Conference Proceedings; AIP Publishing LLC, 2021020001.
(31) Yan, X.; Qian, J.; Pei, X.; et al. Enhanced photodegradation of doxycycline (DOX) in the sustainable $NiFe_2O_4$/MWCNTs/BiOI system under UV light irradiation. *Environ. Res.* **2021**, *199*, No. 111264.
(32) Gan, J.; Zhang, J.; Zhang, B.; et al. Active sites engineering of Pt/CNT oxygen reduction catalysts by atomic layer deposition. *J. Energy Chem.* **2020**, *45*, 59−66.
(33) Ali, N.; Taha, A.; Ahmed, D. S. Characterization of Treated Multi-Walled Carbon Nanotubes and Antibacterial Properties. *J. Appl. Sci. Nanotechnol.* **2021**, *1* (2), 1−9.
(34) Eigler, S.; Grimm, S.; Hirsch, A. Investigation of the thermal stability of the carbon framework of graphene oxide. *Chem. - Eur. J.* **2014**, *20* (4), 984−989.
(35) Lee, D.; Yang, H.; Park, S.; Kim, W. Nafion/graphene oxide composite membranes for low humidifying polymer electrolyte membrane fuel cell. *J. Membr. Sci.* **2014**, *452*, 20−28.
(36) Song, Y.; Zhu, J.; Xu, H.; et al. Synthesis, characterization and visible-light photocatalytic performance of Ag_2CO_3 modified by graphene-oxide. *J. Alloys Compd.* **2014**, *592*, 258−265.
(37) Shan, L.; Bi, J.; Lu, C.; Xiao, Y. $BiVO_4$ (010)/rGO Nanocomposite and Its Photocatalysis Application. *J. Inorg. Organomet. Polym. Mater.* **2019**, *29*, 1000−1009.
(38) Ye, S.; Xu, Y.; Huang, L.; et al. MWCNT/$BiVO_4$ photocatalyst for inactivation performance and mechanism of Shigella flexneri HL, antibiotic-resistant pathogen. *Chem. Eng. J.* **2021**, *424*, No. 130415.
(39) Zhao, D.; Wang, W.; Sun, Y.; et al. One-step synthesis of composite material MWCNT@$BiVO_4$ and its photocatalytic activity. *RSC Adv.* **2017**, *7* (53), 33671−33679.
(40) Jihad, M. A.; Noori, F. T.; Jabir, M. S.; Albukhaty, S.; AlMalki, F. A.; Alyamani, A. A. Polyethylene glycol functionalized graphene oxide nanoparticles loaded with nigella sativa extract: a smart antibacterial therapeutic drug delivery system. *Molecules* **2021**, *26* (11), 3067.
(41) Khashan, K. S.; Abdulameer, F. A.; Jabir, M. S.; Hadi, A. A.; Sulaiman, G. M. Anticancer activity and toxicity of carbon nanoparticles produced by pulsed laser ablation of graphite in water. *Adv. Nat. Sci.: Nanosci. Nanotechnol.* **2020**, *11* (3), No. 035010.
(42) Mohammed, M. K.; Mohammad, M.; Jabir, M. S.; Ahmed, D. In *Functionalization, Characterization, and Antibacterial Activity of Single Wall and Multi Wall Carbon Nanotubes*, IOP Conference Series: Materials Science and Engineering; IOP Publishing, 2020; p 012028.
(43) Veloz, J. J.; Alvear, M.; Salazar, L. A. Evaluation of alternative methods to assess the biological properties of propolis on metabolic activity and biofilm formation in *Streptococcus mutans*. *J. Evidence-Based Complementary Altern. Med.* **2019**, *2019*, No. 1524195.
(44) Sun, Z.; Yu, Z.; Liu, Y.; Shi, C.; Zhu, M.; Wang, A. Construction of 2D/2D $BiVO_4$/g-C_3N_4 nanosheet heterostructures with improved photocatalytic activity. *J. Colloid Interface Sci.* **2019**, *533*, 251−258.
(45) Pookmanee, P.; Kojinok, S.; Puntharod, R.; Sangsrichan, S.; Phanichphant, S. Preparation and characterization of $BiVO_4$ powder by the sol-gel method. *Ferroelectrics* **2013**, *456* (1), 45−54.
(46) Zhao, D.; Zong, W.; Fan, Z.; et al. Synthesis of carbon-doped nanosheets m-$BiVO_4$ with three-dimensional (3D) hierarchical structure by one-step hydrothermal method and evaluation of their high visible-light photocatalytic property. *J. Nanopart. Res.* **2017**, *19* (4), 1−16.
(47) Guo-Cong, L.; Zhen, J.; Xi-Bing, Z.; Xian-Feng, L.; Hong, L. Hydrothermal synthesis and photocatalytic properties of Cu-doped $BiVO_4$ microsheets. *Chin. J. Inorg. Mater.* **2013**, *28*, 287−294.
(48) Ma, L.; Li, W.-H.; Luo, J.-H. Solvothermal synthesis and characterization of well-dispersed monoclinic olive-like $BiVO_4$ aggregates. *Mater. Lett.* **2013**, *102-103*, 65−67.
(49) Sun, J.; Chen, G.; Wu, J.; Dong, H.; Xiong, G. Bismuth vanadate hollow spheres: Bubble template synthesis and enhanced photocatalytic properties for photodegradation. *Applied Catal., B* **2013**, *132-133*, 304−314.
(50) Wang, X.; Li, G.; Ding, J.; Peng, H.; Chen, K. Facile synthesis and photocatalytic activity of monoclinic $BiVO_4$ micro/nanostructures with controllable morphologies. *Mater. Res. Bull.* **2012**, *47* (11), 3814−3818.
(51) Zhu, G.; Que, W. Hydrothermal synthesis and characterization of visible-light-driven dumbbell-like BiVO4 and Ag/$BiVO_4$ photocatalysts. *J. Cluster Sci.* **2013**, *24* (2), 531−547.
(52) Obaid, Z. S. Physical Properties of PMMA/ZnO Composite Material, Ph.D. Dissertations, University Al-Narhrain2017.
(53) Al-Ammar, K.; Hashim, A.; Husaien, M. Synthesis and study of optical properties of (PMMA-CrCl2) composites. *Chem. Mater. Eng.* **2013**, *1* (3), 85−87.
(54) Sathish, M.; Viswanathan, B.; Viswanath, R.; Gopinath, C. S. Synthesis, characterization, electronic structure, and photocatalytic activity of nitrogen-doped TiO_2 nanocatalyst. *Chem. Mater.* **2005**, *17* (25), 6349−6353.
(55) Liu, B.; Li, Z.; Xu, S.; Ren, X.; Han, D.; Lu, D. Facile in situ hydrothermal synthesis of $BiVO_4$/MWCNTs nanocomposites as high performance visible-light driven photocatalysts. *J. Phys. Chem. Solids* **2014**, *75* (8), 977−983.
(56) Sun, T.; Cui, D.; Ma, Q.; Peng, X.; Yuan, L. Synthesis of $BiVO_4$/MWCNT/Ag@ AgCl composite with enhanced photocatalytic performance. *J. Phys. Chem. Solids* **2017**, *111*, 190−198.
(57) Zhang, M.; Shao, C.; Li, X.; et al. Carbon-modified $BiVO_4$ microtubes embedded with Ag nanoparticles have high photocatalytic activity under visible light. *Nanoscale* **2012**, *4* (23), 7501−7508.
(58) Zhao, Z.; Dai, H.; Deng, J.; Liu, Y.; Au, C. T. Enhanced visible-light photocatalytic activities of porous olive-shaped sulfur-doped $BiVO_4$-supported cobalt oxides. *Solid State Sci.* **2013**, *18*, 98−104.
(59) Song, H.; Sun, J.; Shen, T.; Deng, L.; Wang, X. Insights into the mechanism of the Bi/$BiVO_4$ composites for improved photocatalytic activity. *Catalysts* **2021**, *11* (4), 489.
(60) Liu, B.; Zeng, H. C. Mesoscale organization of CuO nanoribbons: formation of "dandelions. *J. Am. Chem. Soc.* **2004**, *126* (26), 8124−8125.

https://doi.org/10.1021/acsomega.3c04722
ACS Omega 2023, 8, 37147−37161

(61) Kale, B. B.; Baeg, J. O.; Lee, S. M.; Chang, H.; Moon, S. J.; Lee, C. W. $CdIn_2S_4$ nanotubes and "Marigold" nanostructures: a visible-light photocatalyst. *Adv. Funct. Mater.* **2006**, *16* (10), 1349−1354.
(62) Ajayaghosh, A.; Varghese, R.; Praveen, V. K.; Mahesh, S. Evolution of Nano-to Microsized Spherical Assemblies of a Short Oligo (p-phenyleneethynylene) into Superstructured Organogels. *Angew. Chem.* **2006**, *118* (20), 3339−3342.
(63) Pal, S.; Dutta, S.; De, S. In *A Facile Hydrothermal Approach to Synthesize rGO/$BiVO_4$ Photocatalysts for Visible Light Induced Degradation of RhB Dye*, AIP Conference Proceedings; AIP Publishing LLC, 2018; p 030205.
(64) Tan, H. L.; Wen, X.; Amal, R.; Ng, Y. H. $BiVO_4$ {010} and {110} relative exposure extent: governing factor of surface charge population and photocatalytic activity. *J. Phys. Chem. Lett.* **2016**, *7* (7), 1400−1405.
(65) Tachikawa, T.; Ochi, T.; Kobori, Y. Crystal-face-dependent charge dynamics on a $BiVO_4$ photocatalyst revealed by single-particle spectroelectrochemistry. *ACS Catal.* **2016**, *6* (4), 2250−2256.
(66) Reichel, T.; Mitnacht, M.; Fenwick, A.; Meffert, R.; Hoos, O.; Fehske, K. Incidence and characteristics of acute and overuse injuries in elite powerlifters. *Cogent Med.* **2019**, *6* (1), No. 1588192.
(67) Han, M.; Chen, X.; Sun, T.; Tan, O. K.; Tse, M. S. Synthesis of mono-dispersed m-$BiVO_4$ octahedral nano-crystals with enhanced visible light photocatalytic properties. *CrystEngComm* **2011**, *13* (22), 6674−6679.
(68) Tian, G.; Fu, H.; Jing, L.; Tian, C. Synthesis and photocatalytic activity of stable nanocrystalline TiO2 with high crystallinity and large surface area. *J. Hazard. Mater.* **2009**, *161* (2−3), 1122−1130.
(69) Brown, L.; Wolf, J. M.; Prados-Rosales, R.; Casadevall, A. Through the wall: extracellular vesicles in Gram-positive bacteria, mycobacteria and fungi. *Nat. Rev. Microbiol.* **2015**, *13* (10), 620−630.
(70) Abo El-Yazeed, W.; El-Hakam, S.; Salah, A.; Ibrahim, A. A. Fabrication and characterization of reduced graphene-$BiVO_4$ nano-composites for enhancing visible light photocatalytic and antibacterial activity. *J. Photochem. Photobiol., A* **2021**, *417*, No. 113362.
(71) Saleem, A.; Ahmed, T.; Ammar, M.; Zhang, H.-l.; Xu, H.-b.; Tabassum, R. Direct growth of m-$BiVO_4$@ carbon fibers for highly efficient and recyclable photocatalytic and antibacterial applications. *J. Photochem. Photobiol., B* **2020**, *213*, No. 112070.
(72) Wang, Y.-W.; Cao, A.; Jiang, Y.; et al. Superior antibacterial activity of zinc oxide/graphene oxide composites originating from high zinc concentration localized around bacteria. *ACS Appl. Mater. Interfaces* **2014**, *6* (4), 2791−2798.
(73) Sun, Z.; Yu, Z.; Liu, Y.; Shi, C.; Zhu, M.; Wang, A. Construction of 2D/2D $BiVO_4$/g-C_3N_4 nanosheet heterostructures with improved photocatalytic activity. *J. Colloid Interface Sci.* **2019**, *533*, 251−258.
(74) Safaei, J.; Ullah, H.; Mohamed, N. A.; et al. Enhanced photoelectrochemical performance of Z-scheme g-C_3N_4/$BiVO_4$ photo-catalyst. *Appl. Catal., B* **2018**, *234*, 296−310.
(75) Pookmanee, P.; Kojinok, S.; Puntharod, R.; Sangsrichan, S.; Phanichphant, S. Preparation and characterization of $BiVO_4$ powder by the sol-gel method. *Ferroelectrics* **2013**, *456* (1), 45−54.
(76) Wang, Y.-W.; Cao, A.; Jiang, Y.; et al. Superior antibacterial activity of zinc oxide/graphene oxide composites originating from high zinc concentration localized around bacteria. *ACS Appl. Mater. Interfaces* **2014**, *6* (4), 2791−2798.
(77) Jiang, J.; Pi, J.; Cai, J. The advancing of zinc oxide nanoparticles for biomedical applications. *Bioinorg. Chem. Appl.* **2018**, *2018*, No. 1062562.
(78) Al Rugaie, O.; Jabir, M.; Kadhim, R.; et al. Gold nanoparticles and graphene oxide flakes synergistic partaking in cytosolic bactericidal augmentation: role of ROS and NOX2 activity. *Microorganisms* **2021**, *9* (1), 101.
(79) Ye, S.; Xu, Y.; Huang, L.; Lai, W.; Deng, L.; Lin, Z.; Xie, G.; et al. MWCNT/BiVO4 photocatalyst for inactivation performance and mechanism of Shigella flexneri HL, antibiotic-resistant pathogen. *Chem. Eng. J.* **2021**, *424*, No. 130415.
(80) Saleem, A.; Ahmed, T.; Ammar, M.; Zhang, H. L.; Xu, H. B.; Tabassum, R. Direct growth of m-BiVO4@ carbon fibers for highly efficient and recyclable photocatalytic and antibacterial applications. *J. Photochem. Photobiol., B* **2020**, *213*, No. 112070.
(81) Manikandan, V.; Mahadik, M. A.; Hwang, I. S.; Chae, W. S.; Ryu, J.; Jang, J. S. Visible-light-active CuO x-loaded Mo-BiVO4 photo-catalyst for inactivation of harmful bacteria (*Escherichia coli* and *Staphylococcus aureus*) and degradation of orange II Dye. *ACS Omega* **2021**, *6* (37), 23901−23912.
(82) Jabir, M. S.; Nayef, U. M.; Jawad, K. H.; Taqi, Z. J.; Ahmed, N. R. In *Porous Silicon Nanoparticles Prepared via an Improved Method: A Developing Strategy for a Successful Antimicrobial Agent Against Escherichia coli and Staphylococcus aureus*, IOP Conference Series: Materials Science and Engineering; IOP Publishing, 2018012077.
(83) Aymen, N.; Aqib, A. I.; Akram, K.; Majeed, H.; Murtaza, M.; Muneer, A.; Alsayeqh, A. F. Resistance modulation of dairy milk borne *Streptococcus agalactiae* and *Klebsiella pneumoniae* through metallic oxide nanoparticles. *Pak. Vet. J.* **2022**, *42* (3), 424−428.
(84) Kandeel, M.; Rehman, T. U.; Akhtar, T.; Zaheer, T.; Ahmad, S.; Ashraf, U.; Omar, M. Antiparasitic applications of nanoparticles: a review. *Pak. Vet. J.* **2022**, *42* (2), 135−140.
(85) Jalil, P. J.; Shnawa, B. H.; Hamad, S. M. Silver nanoparticles: green synthesis, characterization, blood compatibility, and proto-scolicidal efficacy against *Echinococcus granulosus*. *Pak. Vet. J.* **2021**, *41* (3), 393−399.
(86) Shnawa, B. H.; Jalil, P. J.; Aspoukeh, P.; Mohammed, D. A.; Biro, D. M. Protoscolicidal and biocompatibility properties of biologically fabricated zinc oxide nanoparticles using Ziziphus spina-christi leaves. *Pak. Vet. J.* **2022**, *42* (4), 517−525.
(87) Aziz, S.; Abdullah, S.; Anwar, H.; Latif, F. DNA damage and oxidative stress in economically important fish, Bighead carp (*Hypophthalmichthys nobilis*) exposed to engineered copper oxide nanoparticles. *Pak. Vet. J.* **2022**, *42* (1), 1−8.
(88) Aziz, S.; Abdullah, S.; Anwar, H.; Latif, F.; Mustfa, W. Effect of engineered nickel oxide nanoparticles on antioxidant enzymes in fresh water fish, Labeo rohita. *Pak. Vet. J.* **2021**, *41* (3), 424−428.
(89) Khan, I.; Zaneb, H.; Masood, S.; Ashraf, S.; Rehman, H. F.; Rehman, H. U.; Ahmad, S.; Taj, R.; Rahman, S. U. Supplemental selenium nanoparticles-loaded to chitosan improves meat quality, pectoral muscle histology, tibia bone morphometry and tissue mineral retention in broilers. *Pak. Vet. J.* **2022**, *42* (2), 236−240.

https://doi.org/10.1021/acsomega.3c04722
ACS Omega 2023, 8, 37147−37161